Asian Journal of Pharmaceutical Sciences 19 (2024) 100938

Available online at www.sciencedirect.com

ScienceDirect

journal homepage: www.elsevier.com/locate/AJPS

Research Article

Rational fusion design inspired by cell-penetrating peptide: SS31/S-14 G Humanin hybrid peptide with amplified multimodal efficacy and bio-permeability for the treatment of Alzheimer's disease

Kang Qian[a], *Peng Yang*[a], *Yixian Li*[a], *Ran Meng*[a], *Yunlong Cheng*[a], *Lingling Zhou*[a], *Jing Wu*[a], *Shuting Xu*[a], *Xiaoyan Bao*[b], *Qian Guo*[a], *Pengzhen Wang*[a], *Minjun Xu*[a], *Dongyu Sheng*[a], *Qizhi Zhang*[a,*]

[a] *Key Laboratory of Smart Drug Delivery, Ministry of Education, School of Pharmacy, Fudan University, Shanghai 201203, China*
[b] *School of Pharmaceutical Sciences, Wenzhou Medical University, Wenzhou 325035, China*

ARTICLE INFO

Article history:
Received 3 August 2023
Revised 26 December 2023
Accepted 16 May 2024
Available online 24 June 2024

Keywords:
Hybrid peptide
S-14 G Humanin
SS31
Permeability
Aβ
Alzheimer's disease

ABSTRACT

Alzheimer's disease is a neurodegenerative disease induced by multiple interconnected mechanisms. Peptide drug candidates with multi-modal efficacy generated from fusion strategy are suitable for addressing multi-facet pathology. However, clinical translation of peptide drugs is greatly hampered by their low permeability into brain. Herein, a hybrid peptide HNSS is generated by merging two therapeutic peptides (SS31 and S-14 G Humanin (HNG)), using a different approach from the classical shuttle-therapeutic peptide conjugate design. HNSS demonstrated increased bio-permeability, with a 2-fold improvement in brain distribution over HNG, thanks to its structure mimicking the design of signal peptide-derived cell-penetrating peptides. HNSS efficiently alleviated mitochondrial dysfunction through the combined effects of mitochondrial targeting, ROS scavenging and p-STAT3 activation. Meanwhile, HNSS with increased Aβ affinity greatly inhibited Aβ oligomerization/fibrillation, and interrupted Aβ interaction with neuron/microglia by reducing neuronal mitochondrial Aβ deposition and promoting microglial phagocytosis of Aβ. In 3× Tg-AD transgenic mice, HNSS treatment efficiently inhibited brain neuron loss and improved the cognitive performance. This work validates the rational fusion design-based strategy for bio-permeability improvement and efficacy amplification, providing a paradigm for developing therapeutic peptide candidates against neurodegenerative disease.

* Corresponding author.
E-mail address: qzzhang@fudan.edu.cn (Q. Zhang).
Peer review under responsibility of Shenyang Pharmaceutical University.

https://doi.org/10.1016/j.ajps.2024.100938

1. Introduction

Alzheimer's disease (AD) stands as the most common form of dementia and is swiftly evolving into one of the most burdensome, deadly, and financially demanding diseases of this century [1]. Although the initial cause of AD is still debatable, multiple pathologies, including abnormal deposition of amyloid β-protein (Aβ), mitochondrial dysfunction, and glial cell activation-induced inflammation, jointly catalyze the progression of this disease [2,3]. Protein or peptide-based therapeutic candidates could offer high potency, specificity, and multi-modal efficacy by structural fusion, making them especially suitable for the treatment of AD with complex pathologies [4,5]. However, their large molecular weight and hydrophilicity hindered the penetration across the blood-brain barrier (BBB). Currently, one of the established non-invasive BBB permeation strategies is coupling drug molecules with shuttle molecules such as cell-penetrating peptides (CPPs) or ligands of receptors/transporters overexpressed on BBB [6,7]. However, the targeting parts of shuttle-drug conjugates generally bear no therapeutic effect, and some cationic CPPs may cause hemolytic toxicity and accelerated circulation clearance [8]. Therefore, novel concepts to extend fusion strategy that could simultaneously impart multi-modal efficacy and improve the permeability are pursued.

S14G-Humanin (HNG), a potent version of the Humanin peptide, exerts neuroprotection *via* inhibiting Aβ-related toxicity and activating signal transducer and activator of transcription 3 (STAT3) pathway [9]. Unfortunately, its poor ability to cross the BBB limits its effectiveness [10,11]. In pursuit of enhanced bio-permeability, analysis of secondary structure, segmental charge and hydrophilicity of HNG is critical for further sequence extension/alteration and refinement. Alsanousi et al. found that HNG harbors a general signal peptide structure with a positively charged N-terminus, hydrophobic α-helical middle region, and polar C-terminus [12]. According to the classification of CPPs based on the origins, one class called signal peptides-derived CPPs are generated by covalently attaching cationic nuclear localization sequences (NLSs) to signal peptides, in which case the lysine/arginine/proline-rich nature of the NLSs peptide and central hydrophobic region of the signal peptides are both crucial to the fine uptake profiles of the final hybrid peptide [13,14]. By adopting the similar design principle, linking a cationic therapeutic peptide to HNG may augment the overall molecular permeability and exert a synergistic therapeutic effect against the multiple mechanisms-involved AD.

SS31 (R(d)-Dmt-KF-NH_2), a potent antioxidant peptide with excellent membrane permeability and mitochondria-targeting capability, whose sequence is characterized by alternate cationic and aromatic amino acids, confers similarity to NLSs such as KKRPKP and FKKFRK to some extent [15,16]. In previous study, SS31 was merged with HNG to generate the hybrid peptide HNSS [17]. A neuron-targeting polymeric carrier was developed to deliver HNSS and take advantage of its dual efficacy endowed by SS31 and HNG, while the nature of pure HNSS has been less studied. In this study, we found that SS31 linkage to the N-terminus rather than C-terminus of HNG through a dual glycine linker could compensate for the defect of low positive charge density in the initial HNG's N-terminus, therefore resulting in dramatically improved membrane permeability and amplified antioxidant and neuroprotective effects of both SS31 and HNG, while still being able to localize to mitochondria (Scheme 1). In addition, HNSS exhibited higher Aβ_{42} affinity, thus efficiently inhibiting oligomerization and fibrillation of Aβ_{42}, and reducing its toxicity to neurons and pro-inflammatory activity on microglia. These findings indicate that merging two therapeutic peptides not only integrates the respective pharmacological efficacy to a single molecule entity, but also improves molecule's bio-permeability through rational structure optimization.

2. Materials and methods

2.1. Materials

HNSS (R(d)-Dmt-KFGGMAPRGFSCLLLLTGEIDLPVKRRA-NH2), HNRS (MAPRGFSCLLLLTGEIDLPVKRRAGGR(d)-Dmt-KF-NH2), FITC-HNSS, FITC-HNRS, Cy5-HNSS and Cy5-HNRS were purchased from Top Peptide Biotechnology (China). 2, 2, 2-trifluoroethanol was purchased from Aladdin Co., Ltd. (China). HNG (MAPRGFSCLLLLTGEIDLPVKRRA), FITC-HNG, Cy5-HNG, SS31 (R(d)-Dmt-KF), FITC-SS31 and Cy5-SS31 were purchases from ChinaPeptides Co., Ltd. (China). FAM-Aβ_{42} was purchased from Anaspec Co., Ltd. (USA). Aβ_{42} and FITC-Aβ_{42} were purchased from Chinese Peptide Co., Ltd. (China). Poly-lysine (linear, 4 KDa) was obtained from RuixiBio (China). 1,1′-Dioctadecyl-3,3,3′,3′- Tetramethylindodicarbocyanine, 4-Chlorobenzenesulfonate Salt (DiD) was purchased from Beyotime (China). Filipin, monensin, and 6-Diamidino-2-phenylindole dihydrochloride (DAPI) were purchased from Meilunbio (China). Chlorpromazine, genistein, and brefeldin were purchased from Sigma-Aldrich (USA). Mitotracker Red™, and MitoSOX™ Red were purchased from Thermo Fisher (USA). Primers of TNF-α, IL-1β, and β-actin were purchased from Sangon Biotech (China). ALT, AST, BUN and CRE kit were purchased from Solarbio (China). bEnd.3 cells and HT22 cells were obtained from Chinese Academy of Sciences Cell Bank (China). BV2 cells was purchased from EK-Bioscience (China).

2.2. Animals

ICR mice (male, 20 ± 2 g, Shanghai Sino-British Sippr/BK Lab Animal Ltd., China). Triple-transgenic AD mice (3 × Tg-AD, B6;129-Psen1tm1Mpm Tg(AβPPSwe, tauP301L) 1Lfa/Mmjax, male and female in half, Jackson Laboratory, USA). Age-matched C57BL6 (wild type) mice (Shanghai Model Organisms Center, Shanghai, China). Animals were kept in SPF condition, with twelve-h light/dark circle, 25 °C temperature and 55 % humidity. Animal experiments were conducted with approval (No. 2018–03-YJ-ZQZ-01) of the institutional animal care and use committee (IACUC) of Fudan University.

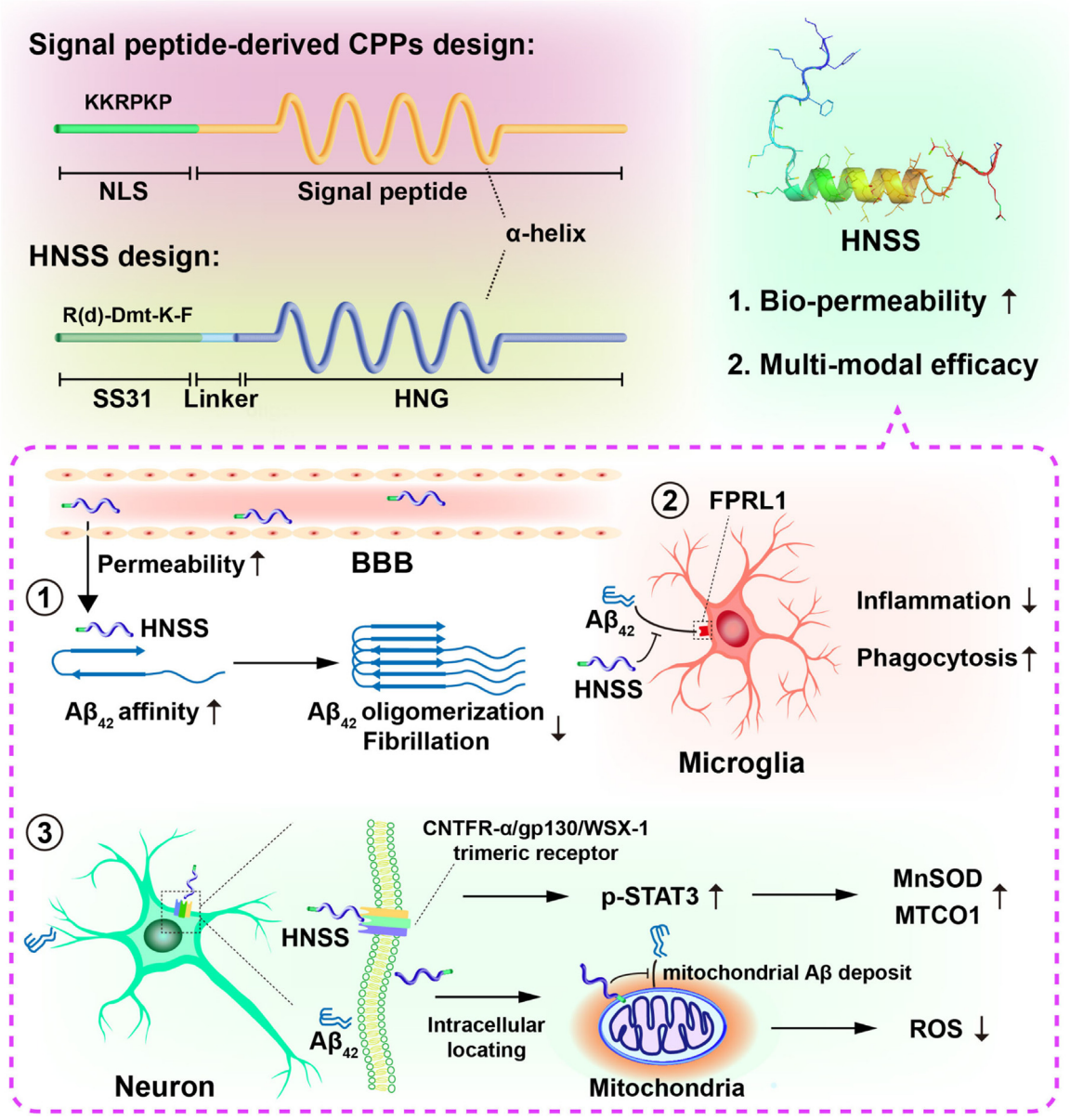

Scheme 1 – Schematic illustration of the design of HNSS and multi-modal therapeutic functions of HNSS against Aβ_{42}, neuron and microglia. (1) HNSS bearing improved Aβ_{42} affinity binds with Aβ_{42} monomer and inhibits Aβ oligomerization and fibrillation. (2) HNSS attenuates microglial inflammation and restores Aβ phagocytosis through formyl peptide receptor like-1 (FPRL1). (3) HNSS exerts neuron protection by activating STAT3 phosphorylation via CNTFR-α/gp130/WSX-1 trimeric receptors, and by intracellular mitochondrial localization to scavenge ROS.

2.3. *Circular dichroism (CD) analysis*

The HNSS, HNG and SS31 were dissolved in 30% (v/v) trifluoroethanol water solution at the concentration of 1 mg/ml. The 400 µl samples were added to 1 mm path length quartz cell and measured by Jasco J-815 spectro-polarimeter (Jasco, Japan) from 190 to 260 nm at the step of 0.1 nm. The spectra were reported out of 3 accumulated scans and subtracted by the baseline of 30% trifluoroethanol water solution. The CD results were shown as the mean residue ellipticity.

2.4. *Structure simulation by AlphaFold2*

The structural prediction of peptides based on the sequence conducted on AlphaFold2 on Google Colab server (https://colab.research.google.com/github/sokrypton/ColabFold/blob/main/AlphaFold2.ipynb accessed on 05/05/2022), which is a slightly simplified version of AlphaFold2 and generates three-dimensional models based on input sequences [18]. AlphaFold2 is only applicable for prediction of sequence containing only natural amino acid, so the R(d) (D-configuration arginine) and Dmt (2′,6′-

dimethyl tyrosine) in HNSS and HNRS sequences are changed to L-configuration arginine and tyrosine. The input sequences were RYKFGGMAPRGFSCLLLLTGEIDLPVKRRA and MAPRGFSCLLLLTGEIDLPVKRRAGGRYKF, respectively. Five best conformations were generated and template was used. Peptide conformation with the highest Local Distance Difference Test (LDDT) score was selected and shown.

2.5. In vitro *cellular uptake in bEnd.3 cells*

The bEnd.3 cells were seeded (5×10^4 /cm^2) in glass-bottom 24-well cell plate and incubated for 24 h. Blank bEnd.3 cells or poly-lysine (4 KDa, 20 μM, 1 h)-treated bEnd.3 were incubated with 10 μM free FITC, FITC-HNSS, FITC-HNRS, FITC-HNG and FITC-SS31 solution for 10 min, 30 min or 2 h. Then bEnd.3 cells were washed with cold PBS three times and fixed with 4% paraformaldehyde. After staining by 10 μM DiD for 30 min or 10 μg/ml Hoechst 33,342 for 10 min, the cells were observed by laser confocal microscope (Zeiss LSM 710, Germany).

For quantitative analysis, bEnd.3 cells were seeded and incubated with each FITC-labelled peptide as described above. After PBS washing and trypsinization, the cells were suspended in 0.2 ml PBS and analyzed by CytoFlex S flow cytometer (Ex=488 nm, Em=525 nm. Beckman Coulter, USA).

2.6. *Cellular uptake mechanism in bEnd.3 cells*

The bEnd.3 cells were seeded (5×10^4 /cm^2) in 24-well cell plate and incubated for 24 h. The bEnd.3 cells were incubated for 30 min with each inhibitor: filipin (caveolae-mediated endocytosis, 10 μg/ml), chlorpromazine (clathrin-mediated endocytosis, 20 μg/ml), brefeldin A (Golgi apparatus, 20 μg/ml), monensin (lysosome, 100 nM), M-β-cyclodextrin (lipid raft, 10 mM), or colchicine (microtubules, 4 μg/ml). The FITC-HNSS (1 μM) was then added to each well and incubated at 37 °C or 4 °C for 2 h. After PBS washing and trypsinization, the cells were suspended in 0.2 ml PBS and analyzed by CytoFlex S flow cytometer (Ex=488 nm, Em=525 nm. Beckman Coulter, USA).

2.7. *Penetration of* in vitro *BBB transwell model*

The *in vitro* BBB model was established by bEnd.3 in transwell system (24-well, 0.4 μm pore, Corning, USA). The bEnd.3 cells were seeded in upper chamber (10^5/well) and allowed to grow for 14 d The formation of bEnd.3 monolayer with transepithelial electrical resistance (TEER) value $\geq$200 Ω·cm^2 was confirmed by Millicell volt-ohmmeter (Millipore, USA). 10 μM free FITC, FITC-HNSS, FITC-HNG, FITC-HNRS, and FITC-SS31 dissolved in FBS-free DMEM was added into the upper chamber and incubated for 2 h. The bEnd.3 monolayer was washed with PBS (3 times), then fixed with 4% paraformaldehyde and stained by 10 μg/ml Hoechst 33,342. The fluorescence distribution in bEnd.3 monolayer was observed by laser confocal microscope (LSM 710, Zeiss, Germany).

2.8. *Ex vivo distribution*

ICR mice were intravenously injected with Cy5-labelled SS31, HNG and HNSS at the dose of 0.5 μMol/kg. At 20 min post injection, mice were anesthetized with isoflurane and heart-perfused with saline and 4% paraformaldehyde. The brains and other major organs were dissected for imaging with IVIS Spectrum Imaging System (Caliper PerkinElemer, USA).

2.9. *Intracellular localization of HNSS in HT22 cells*

The HT22 cells were seeded (5×10^4 /cm^2) in poly-lysine-coated glass-bottom culture dish and were incubated for 24 h. 10 μM FITC-SS31, FITC-HNG and FITC-HNSS dissolved in FBS-free DMEM were added and incubated for 2 h. Then drug-containing DMEM was discarded and HT22 cells were incubated with 300 nM Mitotracker Red for 30 min at 37 °C. After PBS washing and 4% paraformaldehyde fixation, nuclei were stained by 10 μg/ml Hoechst 33,342. HT22 cells were observed by laser confocal microscope (LSM 710, Zeiss, Germany).

2.10. *Mitochondrial ROS observation*

The HT22 cells were seeded (5×10^4 /cm^2) in poly-lysine-coated glass-bottom culture dish and were incubated for 24 h. HT22 cells were treated with 10 μM FITC-SS31, FITC-HNG and FITC-HNSS for 12 h, and then treated with 100 μM H_2O_2 at 37 °C for 6 h. Then 5 μM MitoSOX was added and incubated for 10 min at 37 °C. After PBS washing and 4% paraformaldehyde fixation, nuclei were stained by 10 μg/ml Hoechst 33,342. HT22 cells were observed by laser confocal microscope (LSM 710, Zeiss, Germany. Ex = 510 nm, Em = 580 nm).

2.11. *Microscale thermophoresis*

FITC-Aβ_{42} stock solution was prepared at concentration of 100 nM in PBS. The 16 samples of HNG and HNSS were prepared by 1:1 serial dilutions with highest concentration of 1000 μM and 200 μM for HNG and HNSS, respectively. Then, 10 μl FITC-Aβ_{42} stock PBS solution was mixed with 10 μl peptide solution at various concentrations and incubated at 25 °C for 10 min. After loading to NanoTemper (Munich, Germany) MO-K022 capillaries and mounting to NanoTemper Monolith Nt.115 device, measurements were conducted at the parameters set to 100% blue LED power, high MST power, laser on time for 20 s, and off time for 5 s. Three independent experiments for each sample were conducted and analyzed by MO Affinity Analysis software to obtain K_d values.

2.12. *Thioflavin T (ThT) fluorescence assay*

To obtain Aβ_{42} monomer stock solution, 1 mg Aβ_{42} peptide was dissolved in 1.5 ml 1,1,1,3,3,3-hexafluoro-2-propanol (HFIP) and sonicated for 30 min. Subsequently, the HFIP was dried by nitrogen flow. The remaining Aβ_{42} was further dissolved in DMSO (5 mM) and sonicated for 15 min. The Aβ_{42} monomer stock solution was prepared by diluting the Aβ_{42} DMSO solution with PBS to 50 μM. The HNG, SS31, HNG+SS31 and HNSS peptide (1 or 10 μM) were incubated with Aβ_{42} monomer solution (10 μM) and ThT (5 μM) in 96-well black plates. Aβ_{42} monomer with ThT was set as control. After incubation at 37 °C for 0, 24 and 48 h, the ThT fluorescence was detected by a microplate reader (Ex = 440 nm, Em = 480 nm).

2.13. SDS-PAGE analysis of $A\beta_{42}$ monomer/oligomers

The $A\beta_{42}$ monomer stock solution was prepared as described above. The HNG, SS31, HNG+SS31 and HNSS peptide (10 μM or 2 μM) were incubated with $A\beta_{42}$ monomer (10 μM) at 37 °C for 48 h. Each sample was loaded to 15 % SDS-polyacrylamide gel for electrophoresis (SDS-PAGE). After transfer to PVDF membrane (Millipore, USA), the band was blocked with 5 % bovine serum albumin for 2 h and incubated with anti-$A\beta_{1-16}$ (6E10, Biolegend, 1:200) primary antibody and corresponding HRP-conjugated secondary antibody. The bands of $A\beta_{42}$ monomer and oligomers were visualized by ECL reagent *via* ChemiDoc XRS+ (Bio-Rad, USA).

2.14. Inhibition of mitochondrial $A\beta_{42}$ deposits

The HT22 cells were seeded (5×10^4 /cm^2) in poly-lysine-coated glass-bottom culture dish and were incubated for 24 h. Then, HT22 cells were treated with 2 μM FAM-$A\beta_{42}$ alone or with 10 μM SS31, HNG and HNSS in FBS-free DMEM for 2 h. After PBS washing and trypsinization, cells were suspended in 0.2 ml PBS and analyzed by flow cytometer (Ex=488 nm, Em=525 nm).

For observation of mitochondrial located FAM-$A\beta_{42}$, HT22 cells treated with FAM-$A\beta_{42}$/peptides as described above were further incubated with 300 nM Mitotracker Red for 30 min at 37 °C. After PBS washing and 4 % paraformaldehyde fixation, nuclei were stained by 10 μg/ml Hoechst 33342 and observed by laser confocal microscope. The fluorescence intensity of FAM-$A\beta_{42}$ colocalized with Mitotracker Red fluorescence was semi-quantified by Image J software.

2.15. Effects of HNSS on STAT3 pathway in HT22 cells

The HT22 cells were seeded (5×10^4 /cm^2) in poly-lysine-coated 6-well culture plates and were incubated for 24 h. The cells were treated with 2 μM $A\beta_{42}$ alone or with 10 μM SS31, HNG, SS31+HNG and HNSS at 37 °C for 24 h. After PBS washing thrice, HT22 cells were lysed by 0.5 ml RIPA-containing cocktail of protease and phosphatase inhibitors. Supernatants were collected after 12,000 rpm centrifugation, and protein concentrations were determined by BCA Protein Assay Kit, followed by western blot analysis of p-STAT3, STAT3, MnSOD, and MTCO1 expression.

2.16. Inhibition $A\beta_{42}$-induced inflammation in BV2 cells

The BV2 cells were seeded (5×10^4 /cm^2) in 6-well for 24 h. BV2 cells were treated with 2 μM $A\beta_{42}$ alone or with 10 μM SS31, HNG, SS31+HNG and HNSS at 37 °C for 24 h. The cells were lysed using RIPA and NLRP3 expression was analyzed by western blot analysis.

2.17. Promotion of Aβ clearance in BV2 cells

The BV2 cells in 24-well plates were treated with 2 μM $A\beta_{42}$ alone or with 10 μM SS31, HNG, SS31+HNG and HNSS at 37 °C for 24 h. Blank DMEM-treated BV2 cells were set as control. After PBS washing for 3 times, each well was incubated with 2 μM FAM-$A\beta_{42}$ for 2 h. After PBS washing and trypsinization, cells were suspended in 0.2 ml PBS and FAM-$A\beta_{42}$ intensity was analyzed by flow cytometer.

2.18. Animal treatment

The wild type (WT) and 3 × Tg-AD mice (10 months, $n = 7$/group, 3 males and 4 females per group) were divided into 4 groups. Each group was intravenously administered with saline (WT and AD group) or peptide solutions: 88.4 nMol/kg/d HNG and SS31 solution (HNG+SS31 group), 88.4 nMol/kg/d HNSS solution (HNSS group). Each group was treated consecutively for 28 d.

2.19. Morris water maze

The WT and 3 × Tg-AD mice after 22-d treatment were subjected to Morris water maze (MWM) test. Briefly, a circular water pool (60 cm diameter) with four quadrants (I-IV) was filled with white-stained water (21 ± 2 °C), and a 9 cm platform was placed 2 cm underwater in the IV quadrant. During a 6-d platform-seeking training, mice were released from borders of 4 quadrants every day, and the time required to reach the platform was recorded as escape latency. Mice unable to reach platform within 60 s were manually guided to platform with a 10-s stay, and the escape latency time in this case was recorded as 60 s. After 6-d training, the underwater platform was removed for probe trial, the mice were released at the border of the II quadrant, and swimming paths of each mouse in 60 s were recorded. The corresponding parameter, including platform-crossing times and distance in target quadrant, were analyzed by Water Maze video-tracking system (Coulbourn, USA).

2.20. Western blotting

The HT22, BV2 cells or hippocampus tissue of mice after treatment were lysed by RIPA containing cocktail of protease and phosphatase inhibitors. Supernatant were collected after 12,000 rpm centrifugation and analyzed by BCA kit. Each sample was loaded to 15 % SDS-polyacrylamide gel for electrophoresis. After transfer to PVDF membrane (Millipore, USA), the band was blocked with 5 % bovine serum albumin for 2 h and incubated with primary antibody: anti-p-STAT3 (1:1000, Abcam), anti-STAT3 (1:1000, Abcam), anti-MnSOD (1:1000, Abcam), anti-MTCO1(1:1000, Abcam), and anti-NLRP3 (1:1000, Abcam) primary antibody. After TBST washing, the bands were incubated with corresponding HRP-conjugated secondary antibody. Then bands of target proteins were visualized by ECL reagent *via* ChemiDoc XRS+ (Bio Rad, USA).

2.21. TEM observation of neuronal mitochondria

The 3 × Tg-AD mice after treatment were anesthetized with isoflurane and cardiac perfused by saline and 2.5 % glutaraldehyde PB buffer. About 1 mm^3 tissue was dissected from CA1 area of mice hippocampus, and further fixed in 4 % paraformaldehyde and 2.5 % glutaraldehyde PB buffer for 24 h at 4 °C. Following 1 % osmium tetroxide fixation, dehydration and epoxy resin embedment, the tissue section

(70 nm) were prepared and stained by uranyl acetate-lead citrate. Mitochondrial morphology of neurons were visualized by transmission electron microscope (TEM, Tecnai G2 F20 S-TWIN, FEI, USA).

2.22. Immunohistochemical staining

The paraffin-embedded brain slices were deparaffinized and hydrated. After antigen retrieval in sodium citrate buffer (95 °C, 10 min), the slices were blocked by goat serum and incubated with Anti-Aβ_{42} (Biolegend, 1:200) primary antibody for 1 h and HRP-conjugated secondary antibody (Abcam, 1:200) for 1 h. Then slices were stained with DAB reagent and counterstained with hematoxylin solution. Following dehydration and coverslipping, the slices were observed by microscope (Leica DMI 4000B, Germany).

2.23. Immunofluorescence staining

The brain slices of mice were blocked with goat serum following 0.3 % Triton X100 perforation. Then each slice was stained with Anti-Aβ_{42} (Biolegend, 1:200), Anti-Iba1 (Abcam, 1:200), Anti-GFAP (Abcam, 1:200) primary antibody and Alexa Fluor 488 or 594 labelled secondary antibody, followed by DAPI (1 μg/ml) staining. Fluorescence images were captured by confocal laser scanning microscope.

2.24. RT-PCR analysis

For mRNA extraction, hippocampus tissue of mice after treatment were added 1 ml cold Trizol. Reverse-transcription to cDNA was conducted using Hifair II 1st strand cDNA synthesis kit (Yeasen, China). PCR amplifications were conducted on QuantStudio3 (Appliedbiosystems, USA) following adding primers and reagents form qPCR SYBR Green Master Mix kit (Yeasen, China). The relative mRNA level of TNF-α and IL-1β were calculated by $2^{-\Delta\Delta Ct}$ method with β-actin for normalization. The primers' sequences include: TNF-α F: GTTCTATGGCCCAGACCCTCAC, R: GGCACCACTAGTTGGTTGTCTTTG; IL-1β, F: TCCAGGATGA GGACATGAGCAC, R: GAACGTCACACACCAGCAGGTTA; β-actin, F: CCACACCCCGCCAGTTC, R: GACCCATACCCACCATCACACC.

2.25. H&E staining

The brain slices of mice were stained with hematoxylin-eosin (H&E) following standard protocol. Images of morphology of neurons in hippocampal area were captured by microscope, the area percentage of pyknotic neuron were analyzed by Image J software. In addition, the major organs, including the heart, liver, spleen, lungs and kidneys, were harvested for H&E staining to assess organ safety.

2.26. Statistical analysis

Data were presented as mean ± SD, unless otherwise stated. Statistical significance ($P < 0.05$) was calculated by one-way ANOVA analysis with Turkey post hoc tests for multiple comparisons.

3. Results and discussion

3.1. Peptide design and characterization

Two hybrid peptides HNSS and HNRS were generated by linearly conjugating prototypical peptide SS31 and HNG through a bi-glycine linker, with SS31 part that was attached to the N- or C-terminus of HNG, respectively. The molecular weight of the prototypical peptides and two hybrid peptides were verified by LC-MS, and their net charge and theoretical pI were shown in Fig. 1A.

To monitor the change of secondary structure after peptide hybridization, each peptide was investigated by CD spectroscopy in a 30 % trifluoroethanol/water medium (membrane-mimicking environment) (Fig. 1B). The CD spectra of SS31 exhibited strong negative peak around 200 nm, indicating random coil conformation which is typical for short peptide containing only four amino acids [19]. Meanwhile, HNG's α-helix conformation was revealed by the negative peak at about 220 nm, being consistent with prior report of α-helix structure in its P3-G14 region [20]. Noteworthily, the CD spectrum of HNG, HNSS and HNRS revealed close molar ellipticity value at 222 nm, suggesting similar α-helical contents for these peptides [21]. Thus, the added sequence (SS31 and glycine linker) did not increase or disrupt the existing α-helical structure of HNG after hybridization into HNSS and HNRS.

Protein/peptide structure prediction by computational methods with Alphafold2 has shown unprecedented accuracy [22-24]. We utilized Alphafold2 to visualize the secondary structure of the hybrid peptides HNSS and HNRS (Fig. 1C), and the predicted conformations were compared with the parent peptide HNG's conformation determined by NMR. HNG's secondary structure harbors three segments (part a-c), including a central α-helix (part b, P3-G14) and random coils at both terminuses (part a and c, M1-A2 and E15-A24) [25]. Simulation results of HNSS and HNRS showed that the central α-helix remained unchanged after hybridization, consistent with the CD measurement data. The merged SS31 part did not combine with the HNG's original part a or c sequence to form a new helix or β-sheet structure. Instead, it only extended the pre-existing random coil in the N-terminus of HNSS, or in the C-terminus of HNRS. In addition, we found that the N- or C- terminal hybridization (HNSS or HNRS) resulted in considerable difference in the distribution of positive-charged (basic) amino acids. The number of positive charge of HNG in part a and c were 1 and 3, respectively, but was increased to 3 in part a of HNSS, and to 5 in part c of HNRS (Fig. 1A and 1C), respectively. Such difference in segmental charge density could potentially affect the functions of HNSS and HNRS.

Helical wheel projection was used to examine the amino acids' placement, polarity, and charge status in the α-helix of the HNG, for further identification of structural defects. As shown in Fig. 1D, the α-helix region (P3-G14) of HNG was found to be overall hydrophobic. As mentioned above, the HNG's sequence conforms to the general signal peptide design. Generally, the central hydrophobic helix of signal peptide was assumed to confer membrane affinity to some

A

Peptide	Sequence (N→C)	Mw	pI[b]	Charge
SS31	R(d)-Dmt-KF-NH$_2$[a]	639.74	11.70	3
HNG	MAPRGFSCLLLLTGEIDLPVKRRA	2657.25	9.49	2
HNSS	R(d)-Dmt-KF*GG* MAPRGFSCLLLLTGEIDLPVKRRA-NH$_2$	3392.38	10.29	5
HNRS	MAPRGFSCLLLLTGEIDLPVKRRA *GG* R(d)-Dmt-KF-NH$_2$	3392.38	10.29	5

[a]Dmt is 2',6'-dimethyl tyrosine, [b]pI is theoretical pI

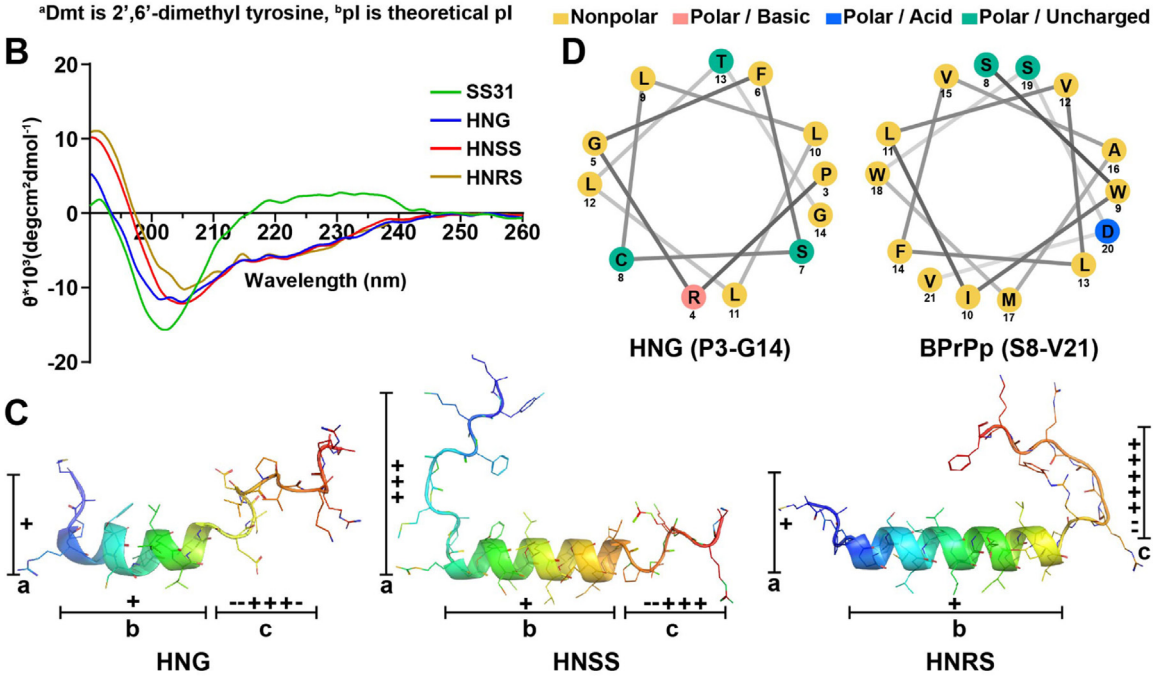

Fig. 1 – Design and characterization of hybrid peptides. (A) The sequences, molecular weight, theoretical isoelectric point and net charge of SS31, HNG, HNSS and HNRS. (B) CD spectroscopy of peptides dissolved in 30 % trifluoroethanol /water. (C) The solution structure of HNG and simulated secondary structures of HNSS and HNRS by Alphafold2. The central helix segments are set as part b, and random coils in N- and C-terminus are set as part a and c. (D) Helical wheel projections of HNG (P3-G14) and BPrPp (S8-V21) peptide generated from *NetWheels* server (http://lbqp.unb.br/NetWheels/).

degree [26]. However, this hydrophobic helix of the signal peptides alone was not enough to generate good membrane permeability, and need to be covalently merged with cationic NLSs to obtain a series of signal peptides-derived CPPs [13]. An example of this category is BPrPp peptide (sequence: MVKSKIGSWILVLFVAMWSDVGLCKKRPKP), bearing a central hydrophobic helix (S8-V21) that is similar to HNG (Fig. 1D), but the terminal NLS-like KKRPKP sequence is essential for its overall cell penetration [27,28]. The absence of an NLS-like sequence inside HHG's structure may account for its poor membrane permeability. Therefore, adding the SS31 sequence to HNG could resolve the structural defect, due to its similarity to the NLSs (*e.g.* SDC3, sequence: FKKFRKF) in terms of lysine/arginine richness [16].

3.2. In vitro *cellular uptake*

As *in vitro* validation of the permeability of the designed peptides, the cellular uptake of the FITC-labelled prototypical peptides and the hybrid peptides were observed by confocal imaging on bEnd.3 cells. As shown in Fig. 2A, the free FITC, FITC-labelled HNG and HNRS only showed weak cellular uptake, whereas SS31 and HNSS exhibited stronger fluorescent signals. Quantitative analysis by flow cytometry also confirmed a similar trend (Fig. 2B), SS31 presented 95.3 % positive rate and 2.6-fold higher fluorescent intensity than that of HNG. Interestingly, HNSS showed even higher fluorescence intensity than that of SS31 (4.2-fold) while exhibiting comparable positive rate. In contrast, HNRS showed modest uptake by bEnd.3 cells, reaching just 1.5-fold of HNG and 13.9 % of HNSS, despite the same molecular weight and total net charge as HNSS.

Further, we observed the adsorption and endocytosis of FITC-labelled peptides in bEnd.3 cells. HNSS and HNRS were both adsorbed on the plasma membrane at 10 min post-incubation (Fig. 2C), but only HNSS was further endocytosed into the cells at the 30-min time point (Fig. 2D). These results, together with the flow cytometry data (Fig. 2B), demonstrated

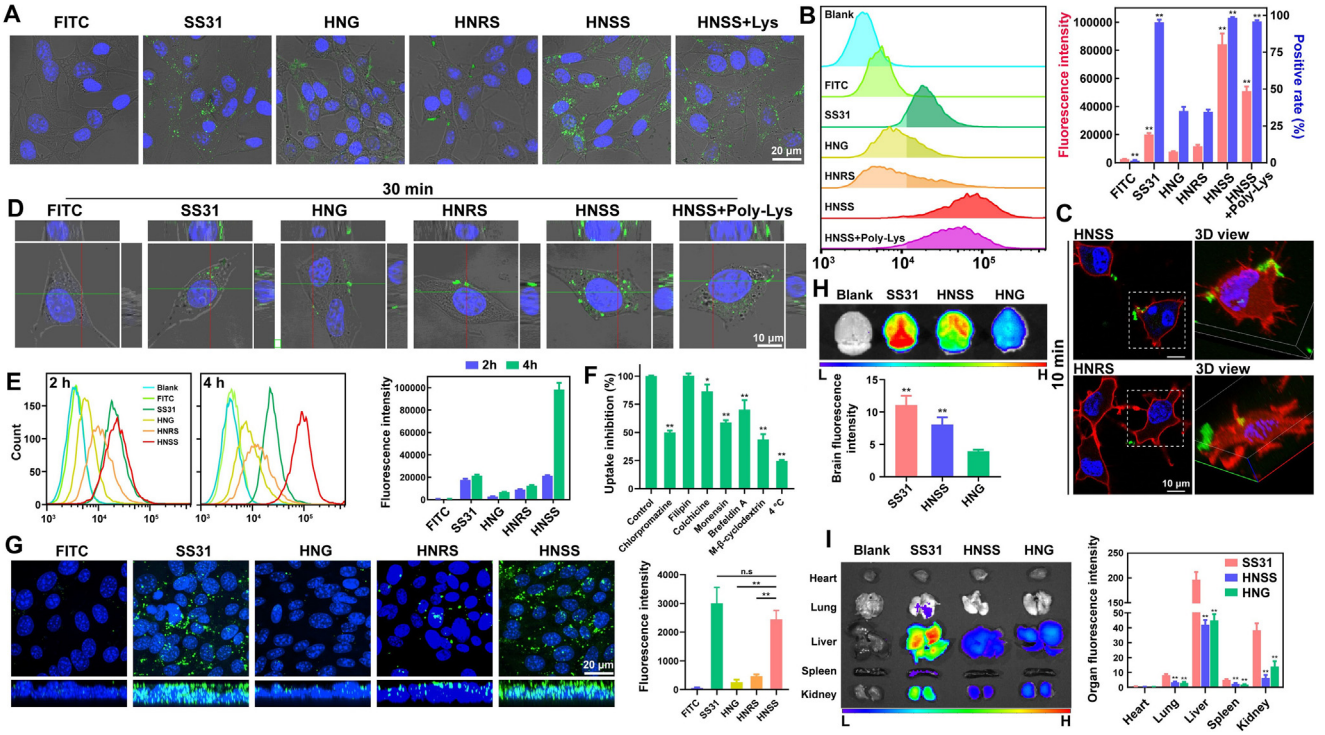

Fig. 2 – *In vitro* uptake comparison, endocytosis mechanism of hybrid peptides and *in vivo* distribution in mice. Blank or poly-lysine-treated bEnd.3 cells were incubated with 10 μM free FITC and FITC labelled HNG, SS31, HNSS or HNRS for 2 h. Representative images (A) and flow cytometry analysis (B) of FITC-peptide uptake. Blank or poly-lysine-treated bEnd.3 cells were incubated with 10 μM free FITC and FITC labelled HNG, SS31, HNSS or HNRS for 10 min (C) or 30 min (D). Blue: nuclei stained with Hoechst 33,342. Green: FITC-labelled peptides. Red: Cell membrane stained with DiD. (C) Microscopic images of peptide adsorption to cell membrane. The right panels represent the three-dimensional view of the area selected by white squares. (D) Representative fluorescence images showing the location of FITC-labelled peptide in bEnd.3 cells, the Z-axis images showing the intracellular position of FITC-labelled peptides in bEnd.3 were placed in the upper and right panels. (E) Flow cytometry analysis of peptide uptake in the presence of FBS. The bEnd.3 cells were incubated with 10 μM FITC-labelled HNG, SS31, HNSS or HNRS in DMEM containing 10 % FBS for 2 h or 4 h. (F) Flow cytometry quantification of effects of different inhibitors on uptake of FITC-HNSS by bEnd.3 cells. The bEnd.3 cells were pre-incubated with inhibitors for 30 min and incubated with 1 μM FITC-HNSS for 2 h at 37 or 4 °C. (G) Microscopic images and semi-quantitative analysis of signal intensity of FITC-labelled peptide in bEnd.3 monolayer. Z-axis images of the peptides penetration into the bEnd.3 monolayer were placed in the lower panels. Blue: nuclei stained with Hoechst 33342. Green: FITC-labelled peptides. (H, I) *Ex vivo* imaging and semi-quantitative analysis of fluorescence intensity in brain and major organs at 20 min after intravenous injection of Cy5-labelled SS31, HNG and HNSS to ICR mice, respectively. Data were presented as mean ± SD ($n = 3$). ns, no significance. *$P < 0.05$, **$P < 0.01$ compared with HNG (B, H), control group (F), HNSS (G) or SS31 (I) group.

that SS31 sequence addition considerably improved the membrane permeability of HNSS, but not of HNRS.

It is worth noting that the positioning of the SS31 motif plays a critical role in conferring disparate cell internalization performance for HNSS and HNRS. As an explanation, HNG contains imbalanced cationic amino acids distribution at its two ends (Fig. 1A and 1C), with the C-terminus (E15-A24) being rich in basic amino acids and the N-terminus (M1-A2) having only one primary amine group. As a result, adding SS31 sequence to the C-terminus just induced skewed positive charge distribution, thus failing to improve the permeability of HNRS. In contrast, SS31 supplemented the positive charge deficiency in N-terminus of HNG and translated into dramatically improved permeability of HNSS.

3.3. *Endocytosis mechanisms exploration in bEnd.3 cells*

Cellular entry of CPPs generally entails multiple pathways, including direct translocation and endocytosis-mediated uptake [29]. In the case of direct translocation, the electrostatic interaction of cationic CPPs with anionic membrane constituents is the first step prior to further membrane translocation. The cationic nature of HNSS contributed to enhanced cellular uptake through electrostatic interaction, as attested by the competition inhibition results with 4 KDa cationic poly-lysine (Fig. 2A, 2B and 2D). However, the abundant endogenous anionic protein may negate this effect by competitive complexation with HNSS. In FBS-containing DMEM, HNSS uptake was inhibited to a level comparable to SS31 at 2 h post-co-incubation (Fig. 2E). However, at 4 h

post-incubation, HNSS regained 4.6-fold higher fluorescence intensity compared with SS31, implying that HNSS uptake is partly dependent on adsorption-mediation while other mechanisms may be involved.

Endocytosis plays an important role in the internalization of CPPs, especially at low concentrations [30]. To explore the possible endocytosis mechanisms, we investigated the inhibitory effect of various inhibitors on HNSS uptake at 1 μM concentration. Results in Fig. 2F proved that HNSS entry into bEnd.3 cells were energy-consuming and involved multiple endocytosis routes including macropinocytosis, lipid raft and clathrin-mediated endocytosis.

3.4. *BBB permeation and ex vivo distribution*

To further validate the potential of HNSS to permeate across BBB, an *in vitro* BBB transwell model composed of monolayer of bEnd.3 cells was established. Confocal fluorescence images of 10 μM FITC-labelled peptides showed that SS31 and HNSS penetrated deeper and passed through the bEnd.3 monolayer (Fig. 2G), with semi-quantitative analysis indicating 11.7- and 9.54-fold higher fluorescence intensity than HNG, respectively. Meanwhile, the fluorescence of HNRS in the bEnd.3 layer was only 1.84-fold of HNG. These results proved that fusion of the SS31 facilitated transcytosis for BBB permeation. As expected, *ex vivo* imaging of brain showed that Cy5-labelled HNSS distribution into brain was 2.04 times higher than that of HNG, and reached 72.5 % of SS31 at 20 min post-injection (Fig. 2H). In other organs, HNSS presented a similar distribution to HNG, while did not exhibit liver and kidney distribution preference as SS31 (Fig. 2I). The fusion strategy for HNSS increased drug permeation across BBB but reduced distribution to peripheral organ; thus, it is suitable for AD treatment.

3.5. *Intracellular localization and anti-oxidative effect of HNSS in HT22 cells*

After entry into brain parenchyma, HNSS uptaken by neurons is expected to be directed to mitochondria under the traction of the SS31 part. Fig. 3A shows the cellular localization of FITC-labelled SS31, HNG, HNSS, and HNRS in HT22 cells and their overlay with the mitochondrial probe Mitotracker Red. The SS31 exhibited mitochondria locating effects as reflected by the R value of 0.62, being consistent with previous reports [31]. HNG barely overlapped with mitochondria (R = 0.05), while HNSS localized to mitochondria (R = 0.58), thus confirming the bestowed mitochondria-targeting ability by the merged SS31 part. In contrast, the HNRS did not accumulate in mitochondria, despite possessing SS31 in its sequence, which can be ascribed to its inability to permeate across the plasma membrane. Based on the superiority of HNSS in both BBB permeability and mitochondrial targeting than HNRS, only HNSS is reserved for further evaluation.

Mitochondria are major production sites of ROS, so the ROS-scavenging effects of prototype and hybrid peptide were measured by MitoSOX probe (Fig. 3B) [32]. Both SS31 and HNG were reported to act directly on mitochondria to alleviate ROS production [33,34]. Here, SS31 was relatively more potent than HNG in eliminating mitochondrial ROS, as it concentrated in mitochondria to locally neutralize ROS [35]. HNG and SS31 co-administration showed lower ROS level than single SS31 and HNG, implying certain synergistic effect. HNSS offered a superior mitochondrial ROS inhibition effect to the co-administration group; the mitochondrial ROS was decreased to 20.8 % of that of the H_2O_2-treated group, proving its strong efficacy against oxidative stress.

3.6. *Neuronal protection of HNSS via p-STAT3 activation in HT22 cells*

The JAK2/STAT3 signaling pathway is critical for HNG-mediated neuroprotection through binding with membrane CNTFR-α/gp130/WSX-1 trimeric receptors [36]. STAT3 inactivation was induced by Aβ_{42} co-incubation in HT22 cells, as shown by the decreased p-STAT3/STAT3 ratio (Fig. 3C). HNSS treatment induced 1.9 and 1.3-fold higher p-STAT3/STAT3 ratio than Aβ_{42} and HNG treated group. Meanwhile, SS31 alone was ineffective in eliciting p-STAT3. We found that the integration of SS31 into HNSS induced 4.1-fold higher membrane-local concentration than HNG (Fig. S1), which facilitated the binding of HNSS to membrane receptors. This could account for HNSS's retained but stronger p-STAT3 activating capability derived from HNG.

According to previous studies, the expression of manganese superoxide dismutase (MnSOD, a mitochondria-located detoxifying enzyme) and respiratory enzymes, especially the complex IV, decrease significantly in AD pathology [37,38]. STAT3 activation could increase the transcription of respiratory enzymes and MnSOD [39-41]. Therefore, expression of cytochrome c oxidase subunit 1 (MTCO1, subunit of complex IV protein) and MnSOD after p-STAT3 activation were monitored. As results show, HNSS upregulated the expression of MnSOD and MTCO1 to 136 % and 111 % of the HNG+SS31 co-administration group, respectively (Fig. 3D). These results collectively reflected the improved mitochondrial functions from various aspects including respiratory enzymes and radical-detoxifying system.

3.7. *Improved Aβ-affinity and anti-oligomerization/fibrillation effects of HNSS*

In solution, Aβ_{42} forms β-sheet conformation and transits to toxic Aβ_{42} oligomers and fibrils [42]. HNG inhibits Aβ_{42} fibrillation by binding with Aβ_{42} and disrupting the β-sheet formation [12]. The binding affinity between Aβ_{42} and HNG or HNSS was firstly determined by microscale thermophoresis (MST). Each peptide at various concentrations was incubated with 50 nM Aβ_{42}, and K_d values were determined from binding curves (Fig. 4A). HNSS demonstrated K_d value of 55.5 ± 12.9 μM, lower than 117.9 ± 23.4 μM of HNG, thus outperformed HNG in terms of Aβ_{42} binding affinity. Molecular docking simulation was further applied to analyze possible interactions [43]. The calculated Aβ_{42} binding affinity value (ΔG) of HNSS was higher than that of HNG (−11.5 kcal/mol *versus* −10.0 kcal/mol, Fig. S2). The arginine (R1) and lysine (K3) residues in the SS31 part of HNSS are involved in the formation of hydrogen bond with Aβ_{42}, and thus may be responsible for the increased binding affinity of HNSS.

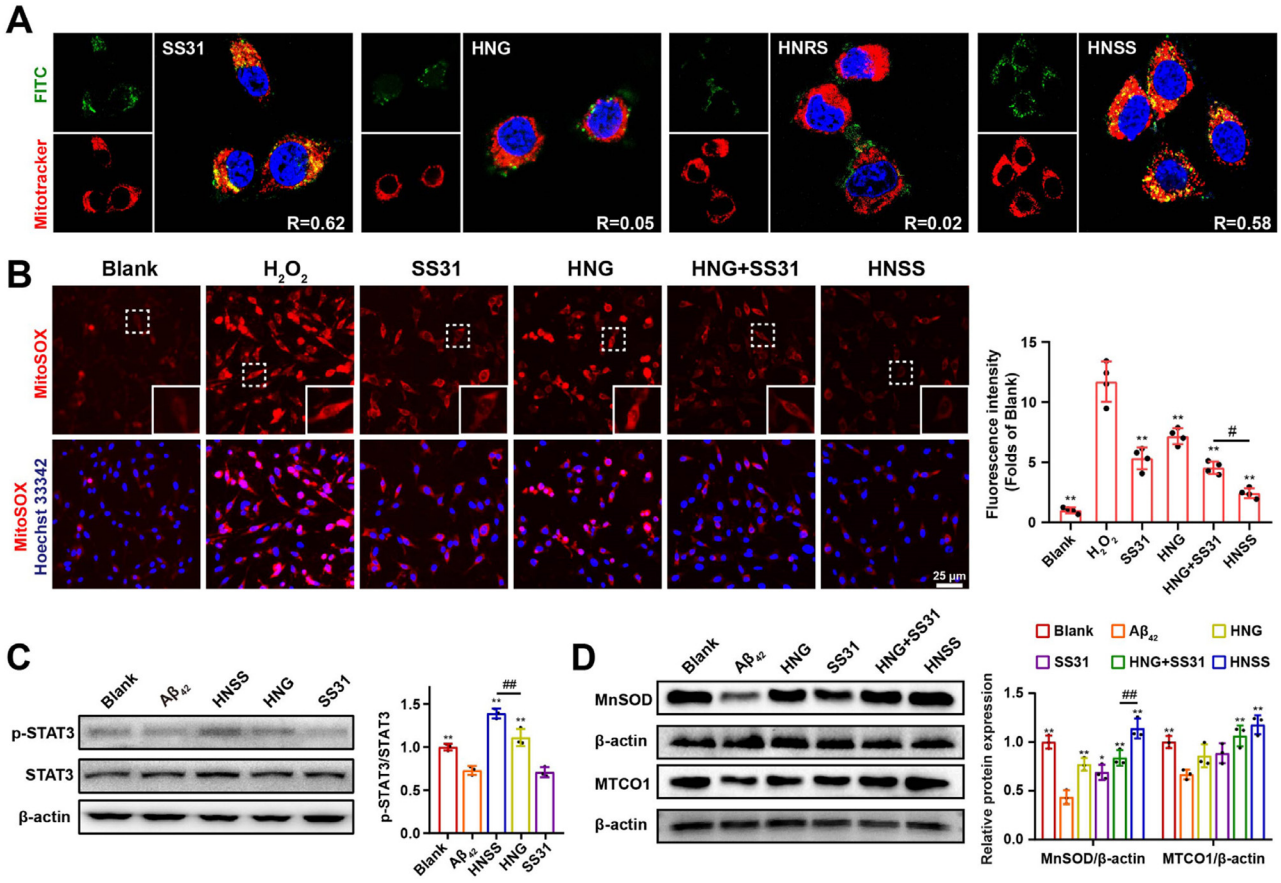

Fig. 3 – Mitochondria targeting, ROS scavenging effects and p-STAT3 activation of HNSS peptide. (A) Subcellular distribution of FITC-labelled peptides in HT22 cells. The HT22 cells were incubated with 10 μM FITC-labelled peptides for 2 h at 37 °C and stained with Mitotracker Red. The Pearson's correlation coefficient (R) was analyzed by Image J. Green: FITC-labelled peptides. Red: Mitotracker Red. (B) Fluorescence micrographs and semi-quantitative analysis of mitochondrial MitoSOX fluorescence. HT22 cells were pre-incubated with 10 μM SS31, HNG, SS31+HNG or HNSS solution for 12 h, and then treated with 100 μM H_2O_2 at 37 °C for 6 h. Red: MitoSOX. Blue: nuclei stained with Hoechst 33342. (C, D) Western blot of p-STAT3, MnSOD, MTCO1 expression in HT22 cells and semi-quantification. HT22 cells were treated with 2 μM $A\beta_{42}$ alone or with 10 μM various peptides at 37 °C for 24 h. Data were presented as mean ± SD. $n = 4$ (B) or 3 (C, D). *P < 0.05, **P < 0.01 compared with H_2O_2 group (B) or $A\beta_{42}$ group (C, D); #P < 0.05, ##P < 0.01, between the compared groups.

ThT fluorescence assay was used to directly reflect the degree of $A\beta_{42}$-fibrillation (Fig. 4B). Incubation of 10 μM $A\beta_{42}$ solution alone showed a rapid conformation transition to fibrils as reflected by the dramatic ThT fluorescence increase within 48 h. The SS31 alone did not affect the $A\beta_{42}$-fibrillation, while 10 μM HNG and HNSS both reduced the ThT fluorescence intensity to the initial level. To further differentiate the relative efficacy of HNG and HNSS, the peptide concentration was reduced to 1 μM, while $A\beta_{42}$ was kept at 10 μM. In this case, the ThT fluorescence at 48 h in the HNSS and HNG groups were 34% and 78% of that in the $A\beta_{42}$ group, respectively, indicating the HNSS's superior $A\beta_{42}$-fibrillation inhibitory efficiency to HNG. Besides the toxic $A\beta_{42}$ fibrils, $A\beta_{42}$ oligomers, especially high-molecule weight (Mw) oligomers, are deemed as more toxic species [44,45], thus, the content change of $A\beta_{42}$ oligomers and monomer was analyzed by $A\beta_{42}$ SDS-PAGE (Fig. 4C and 4D). At the 1:1 $A\beta_{42}$/peptide ratio, the HNSS and HNG-containing group showed higher monomer and lower high-Mw oligomers content compared to the blank $A\beta_{42}$ and SS31-co-incubated group. When the $A\beta_{42}$/peptide ratio was increased to 5:1, although both HNG and HNSS became less effective in inhibiting $A\beta_{42}$ development to high-Mw oligomers than that at 1:1 ratio, HNSS-treated $A\beta_{42}$ presented significantly lower high-Mw oligomer and higher monomer content than HNG+SS31 group.

3.8. *HNSS inhibits neuronal Aβ uptake and deposit on mitochondria*

The $A\beta$ overexpressed by unhealthy neurons could be secreted into extracellular space, and undergo endocytosis through complexing with various receptors, such as receptor for advanced glycation end-products (RAGE), which leads to spread of $A\beta$ toxicity to neighboring neurons [46,47]. Since HNSS effectively binds with $A\beta_{42}$ as shown above, the binding

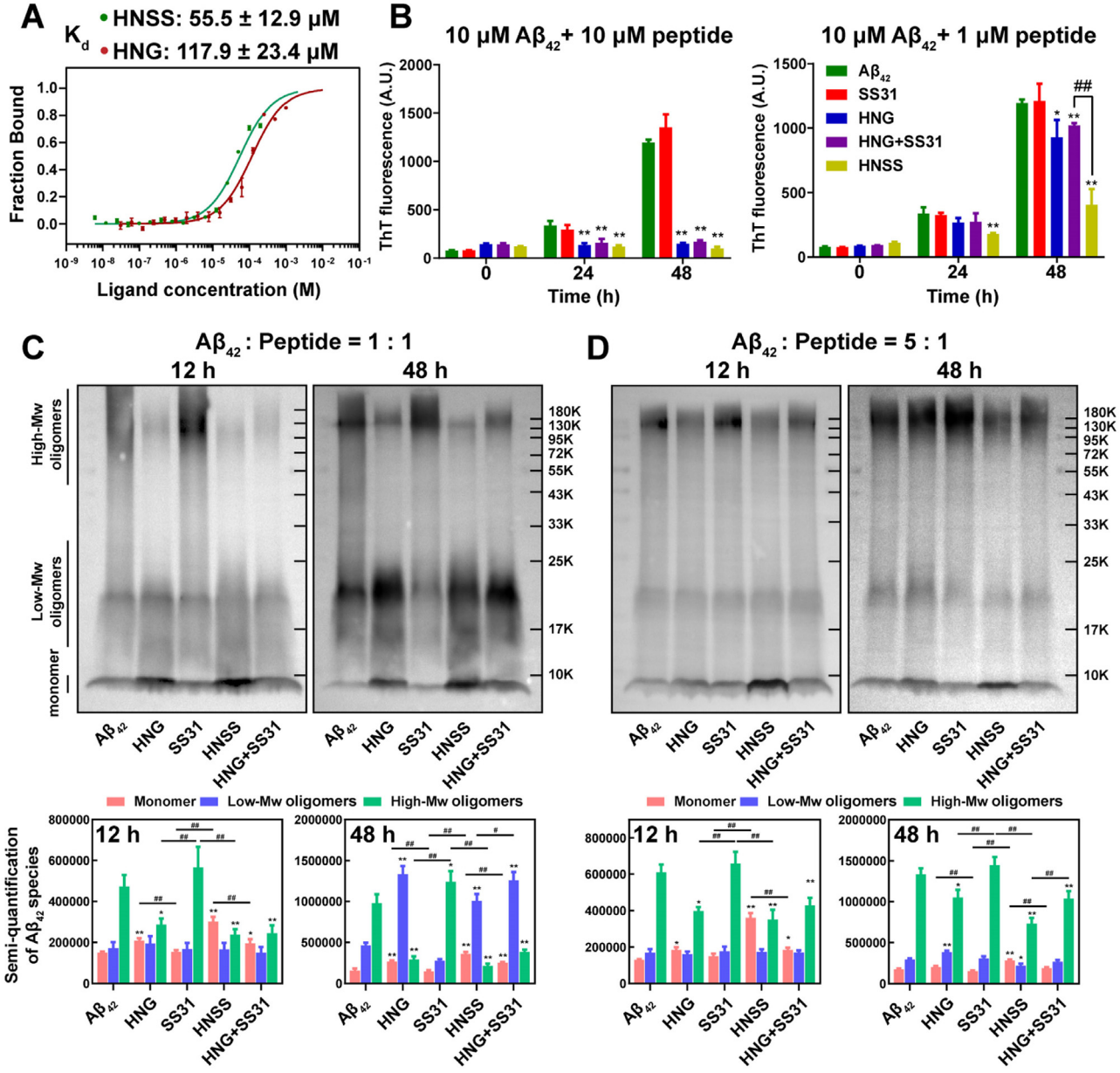

Fig. 4 – The Aβ_{42} fibrillation and oligomerization inhibition effects of HNSS. (A) Bound fraction curves of peptide and Aβ_{42} analyzed by microscale thermophoresis. 50 nM FITC-Aβ_{42} was incubated with different concentrations of HNG or HNSS in PBS. (B) ThT fluorescence intensity of mixture of 10 μM Aβ_{42} and 10 or 1 μM various peptide at 37 °C for 24 h and 48 h. (C, D) Representative SDS-PAGE analysis of Aβ_{42} species. 10 μM Aβ_{42} monomer solution was incubated with 10 μM (C) or 2 μM (D) of various peptides at 37 °C for 12 h or 48 h and were loaded on gel and immunoblotted. Semi-quantification of Aβ_{42} monomer (4 kDa), low-molecular-weight oligomers (~20 kDa) and high-molecular-weight oligomers (48—300 kDa) by Image J. Data were presented as mean ± SD (n = 3). *P < 0.05, **P < 0.01, compared with the blank Aβ_{42} group. #P < 0.05, ##P < 0.01, between the compared groups.

of Aβ_{42} to neurons might compete, so HNSS's effect on neuronal uptake of FAM-labelled Aβ_{42} was analyzed by flow cytometry (Fig. 5A). HNSS co-incubation decreased FAM-Aβ_{42} fluorescence to 17.6 % of the FAM-Aβ_{42}-treated control group, and was also significantly lower than the HNG or HNG/SS31 co-administration group. Correspondingly, cell viability was increased to 81.3 % of normal control after HNSS intervention (Fig. S3).

An important aspect of Aβ toxicity to neurons lies in its deposit in mitochondria and congestion of mitochondrial permeability transition pore (mPTP) or disruption of respiratory function-related enzymes [48]. In FAM-Aβ_{42}-treated HT22 cells, the fluorescence co-localized with mitochondria was intense (Fig. 5B). SS31 co-incubation failed to change such FAM-Aβ_{42} distribution pattern. In comparison, HNG, with moderate Aβ_{42}-binding ability,

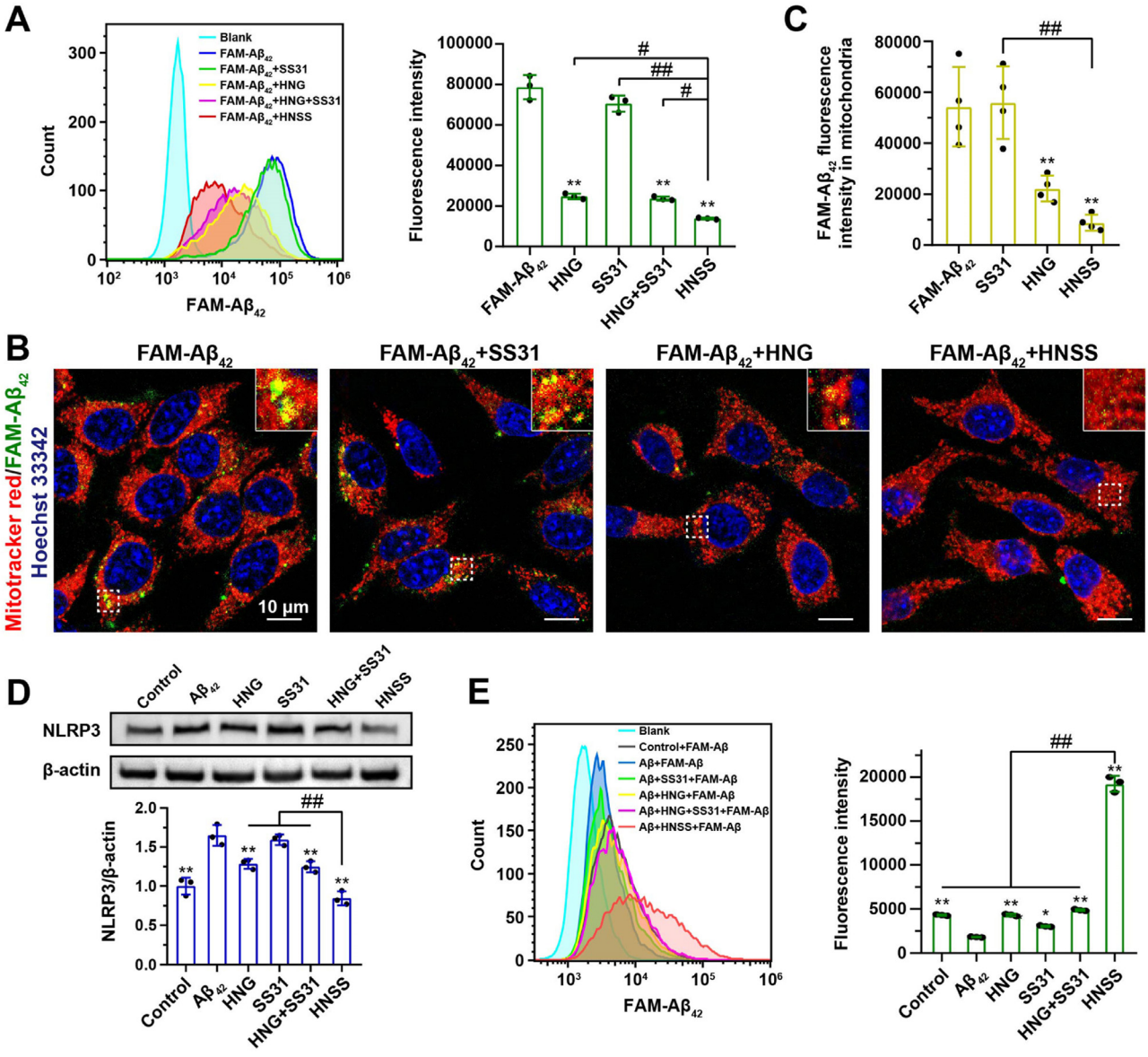

Fig. 5 – Effects of HNSS on neuronal and microglial cells *in vitro*. (A-C) HT22 cells were incubated with 2 μM FAM-Aβ_{42} alone or with 10 μM SS31, HNG, SS31+HNG or HNSS at 37 °C for 2 h, and analyzed by flow cytometry or stained with Mitotracker Red for imaging. (A) Flow cytometry analysis of FAM-Aβ_{42} intensity in HT22 cells. (B) Intracellular location of FAM-Aβ_{42} to mitochondria. Blue: nuclei stained with Hoechst 33,342. Green: FAM-Aβ_{42}. Red: Mitotracker Red. (C) Semi-quantitative analysis of fluorescence intensity of FAM-Aβ_{42} colocalized with mitochondria. (D) Western blot of NLRP3 expression in BV2 and semi-quantification. BV2 cells were treated with 2 μM Aβ_{42} alone or with 10 μM various peptides at 37 °C for 24 h. (E) Flow cytometry analysis of FAM-Aβ_{42} intensity in Aβ_{42}-pretreated BV2 cells. BV2 cells were pre-incubated with 2 μM Aβ_{42} alone or with 10 μM various peptides for 24 h, and were incubated with 2 μM FAM-Aβ_{42} for 2 h. Data were presented as mean ± SD, $n = 3$ (A, D, E) or 4 (C). *P < 0.05, **P < 0.01 compared with Aβ_{42} control; #P < 0.05, ##P < 0.01, between the compared groups.

significantly inhibited FAM-Aβ_{42} co-localization with mitochondria. HNSS, with even higher Aβ_{42} affinity, exhibited the lowest FAM-Aβ_{42} overlap with mitochondria (Fig. 5C). Taking the results above, HNSS bears higher Aβ_{42}-binding affinity, and efficiently interrupts Aβ_{42}/neuron interaction by decreasing neuronal Aβ_{42} uptake and deposits in mitochondria.

3.9. *Inhibition of microglial inflammation and restoration of Aβ phagocytosis*

In healthy conditions, microglia are responsible for the phagocytosis and clearance of toxic proteins, but chronic Aβ stimulation would cause chronic inflammation of microglia, thereby reducing their ability to scavenge toxic Aβ [49,50]. HNG

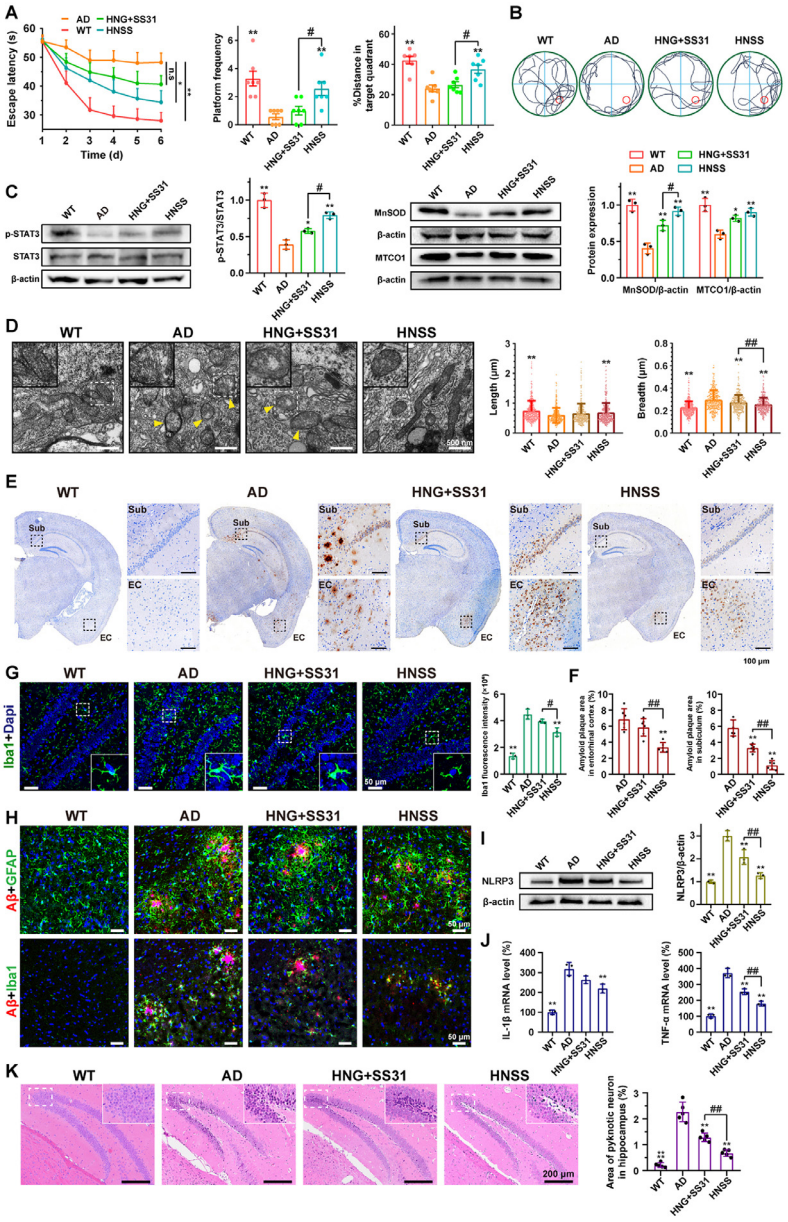

Fig. 6 – Mitochondrial protection, Aβ deposit inhibition, glial activation attenuation and memory improvement by HNSS in 3 × Tg-AD mice. Ten-month old 3× Tg-AD transgenic mice were intravenously injected with saline, HNSS or HNG + SS31 (88.4 nMol/kg/d) for 28 d. WT mice of the same age were injected with saline. (A) Escape latency during 6-d MWM experiment, platform-crossing times and percentage of path in target quadrant after platform removal in probe trial (n = 7). (B) Representative swimming path of AD mice after treatment in probe trial. (C) Western blotting and semi-quantification of p-STAT3, MnSOD and MTCO1 expression in hippocampus of treated male mice (n = 3). (D) Ultrastructure of mitochondria in CA1 area of treated female mice captured by TEM. Yellow arrows: mitochondria with damaged cristae. Length and breadth of mitochondrial TEM images quantified by Image J (n = 312–396 mitochondria from 9 to 12 cells). Representative immunohistochemical images (E) and semi-quantification (F) of the area percentage of Aβ deposit in hippocampus subiculum (Sub) region and entorhinal cortex (EC) (n = 6 regions from 3 to 4 female mice). (G) Representative confocal image of microglia immunostained with anti-Iba1 antibody in hippocampus of treated female mice. Quantitative analysis of optical intensity of Iba1 fluorescence by Image J (n = 3). (H) Representative confocal image of Aβ deposit surrounded by microglia and astrocytes in cortex of treated female mice. Blue: nuclei. Green: Iba1 or GFAP. Red: Aβ deposit. (I) Western blotting and semi-quantification of NLRP3 expression in hippocampus of treated male mice (n = 3). (J) Relative mRNA expression change of IL-1β and TNF-α in hippocampus of treated male mice (n = 3). (K) Representative images of H&E staining of hippocampal dentate gyrus (DG) and semi-quantification of the area percentage of pyknotic neuron with Image J (n = 5 regions from 3 to 4 female mice). Data were presented as mean ± SD, while escape latency (A) was shown as mean ± SEM. *P < 0.05, **P < 0.01 compared with AD group; #P < 0.05, ##P < 0.01, between the compared groups.

was reported to attenuate the microglial activation through formyl peptide receptor like-1 (FPRL1) expressed by microglia [51]. Thus, the effects of HNSS on microglial activation and Aβ clearance were clarified. As shown in Fig. 5D, HNSS inhibited Aβ_{42}-stimulated inflammation in BV2 cells, as demonstrated by the significantly lower level of NLRP3 in the HNSS-treated BV2 group, which is the inflammasome-related protein [52,53]. BV2 cells with lower inflammation exhibited stronger Aβ_{42} phagocytosis, and HNSS treatment improved uptake of FAM-Aβ_{42} by 10.6-fold compared to the Aβ_{42}-treated BV2 group, and was even superior (4.5-fold) to Aβ_{42}-untreated BV2 cells (Fig. 5E).

3.10. *Spatial memory improvement in 3× Tg-AD mice*

The 10-month-old transgenic mice bearing triple mutated human APP(Swe), tau(P301L) and PS1(M146V) genes were intravenously administered with saline, HNSS and HNG+SS31 for 28 d. The spatial memory performance was evaluated by MWM experiment [54]. After 6-d training, the escape latency of WT, HNSS, HNG+SS31 and AD group was 28.0 ± 2.8 s, 34.4 ± 4.1 s, 40.6 ± 3.0 s and 48.3 ± 3.2 s, respectively. The HNSS group showed significantly shorter escape latency than AD group, while HNG+SS31 group was not significant (Fig. 6A). In probe trials when the platform was removed, the paths of HNSS-treated mice showed bias distribution in the target quadrant, as reflected by the larger numbers of platform-crossing and more percentage of swimming distance (Fig. 6A and 6B). These results exhibited the superior memory improvement effects of HNSS than the HNG+SS31 co-administration group.

3.11. *Improvement of mitochondrial function and ultrastructure*

With the intensified p-STAT3 activation potency as revealed by *in vitro* cell model, this effect of HNSS was confirmed in the brain of 3 × Tg-AD mice (Fig. 6C). The ratio of p-STAT3/ STAT3 in HNSS group was 137 % and 204 % higher than that in HNG+SS31 and AD group. Consistently, the downstream MTCO1 and MnSOD expression in the HNSS group was normalized to 90.1 % and 91.6 % compared with WT group (Fig. 6C). The ultrastructure of mitochondria in hippocampal CA1 area was observed by TEM (Fig. 6D). The AD group showed typical swollen and shorter morphology, with damaged cristae. Both HNG+SS31 and HNSS treatment alleviated mitochondrial damage to some extent, while HNSS-treated group showed closer mitochondrial parameters to those of the WT group (Fig. 6D). These above results collectively reflected the effectiveness of HNSS in improving mitochondrial respiratory, anti-oxidative function and ultrastructure preservation.

3.12. *Neuron protection by inhibition of amyloid plaque formation and glial activation*

With enhanced Aβ affinity, HNSS has shown efficacy to suppress Aβ_{42}'s oligomerization/fibrillation tendency *in vitro*. To confirm its *in vivo* effect in the brain of AD mice, immunohistochemical staining was applied to visualize amyloid plaque in brain hemisphere. As shown in Fig. 6E, 3× Tg-AD mice exhibited amyloid plaques, especially in hippocampal subiculum (Sub) and entorhinal cortex (EC). HNSS treatment significantly reduced plaque formation, and the plaque area in Sub and EC region were reduced to 19.5 % and 48.7 % of the AD group (Fig. 6F), respectively. The toxic amyloid deposits generally lead to glial cell recruitment and activation [55]. Therefore, consistent with effective Aβ burden amelioration by HNSS intervention, the fluorescence of microglial Iba1 was significantly lower than that of untreated AD mice in the hippocampus, and the microglial morphology reversed from hypertrophic amoeboid to normal, implying inhibited microglial activation (Fig. 6G). Meanwhile, in the near-Aβ deposits area, the recruitment of microglia and astrocytes for Aβ clearance was also improved by HNSS, as reflected by the increased glial cell-deposit colocation (Fig. 6H). This was consistent with above results that HNSS improved microglial phagocytosis of Aβ_{42} *in vitro*. Corresponding with the glial cells inactivation, the NLRP3 expression, mRNA level of IL-1β and TNF-α significantly dropped in HNSS group, which collectively reflected the relieved inflammation status in AD mice brain (Fig. 6I and 6J). As a result of amyloid burden relief, glial cell inactivation and inflammation inhibition, the area percentage of pyknotic neuron was significantly reduced in hippocampal DG area (Fig. 6K), implying the alleviated neuron impairment that could account for the memory improvement after HNSS intervention.

3.13. *Biocompatibility evaluation*

The membrane destabilization-related hemolysis for some cationic peptide is a major obstacle to *in vivo* biocompatibility [56,57]. Thus, the hemolysis assay was conducted for HNSS and 4 KDa poly-lysine (positive control) (Fig. S4). As results, the 4 KDa poly-lysine showed over 10 % hemolysis at a concentration higher than 1 μM. As comparison, the positively charged HNSS caused 3.3 % hemolysis at concentration as high as 10 μM, and negligible hemolysis (<0.86 %) at a concentration lower than 1 μM, while blood HNSS concentration calculated according to dosage was less than 1.2 μM in the treatment of 3× Tg-AD mice. Thus HNSS showing improved permeability does not bring about unfavored hemolysis risk.

After 28-d daily intravenous injection of each peptide, blood was collected for analysis, the indicators including ALT, AST, BUN and CRE of HNSS-treated mice showed no significant difference from WT mice (Fig. S5A), proving unchanged liver and kidney function [58]. Meanwhile, H&E staining images of major organs reflected no detectable histological change (Fig. S5B). These results ensured the preliminary safety of HNSS for long-term AD intervention after intravenous administration.

4. Conclusion

By leveraging the structural traits of HNG and SS31 peptides, a novel peptide, HNSS, was developed using a fusion strategy following the design principles of signal peptide-derived CPPs. This rational design generated the highly permeable

peptide capable of BBB penetration and brain accumulation. HNSS peptide bears the combined efficacy to eliminate ROS, stimulate STAT3 phosphorylation, and interact with Aβ_{42}, thus efficiently relieving oxidative stress, reducing Aβ oligomerization/fibrillation and inhibiting Aβ interaction with neuron/microglia. These effects ultimately translated to mitochondrial recovery, Aβ burden relief, neuron loss inhibition and memory improvement in 3× Tg-AD mice. Our study proved that rational hybridization of two therapeutic peptides could achieve overall bio-permeability optimization and efficacy integration *via* correcting the innate structure defects of parent peptides, which has reference significance for the development of peptide drugs.

Conflicts of interest

The authors declare no conflict of interest.

Acknowledgments

This work was supported by National Natural Science Foundation of China (82273868 and 82073780), and Shanghai Municipal Natural Science Foundation (19ZR1406200). We thank the staff members of the Large-scale Protein Preparation System at the National Facility for Protein Science in Shanghai (NFPS), Zhangjiang Lab, China for providing technical support and assistance in data collection and analysis.

Supplementary materials

Supplementary material associated with this article can be found, in the online version, at doi:10.1016/j.ajps.2024.100938.

REFERENCES

[1] Scheltens P, De Strooper B, Kivipelto M, Holstege H, Chételat G, Teunissen CE, et al. Alzheimer's disease. Lancet 2021;397(10284):1577–90.
[2] Liu PP, Xie Y, Meng XY, Kang JS. History and progress of hypotheses and clinical trials for Alzheimer's disease. Signal Transduction Targeted Ther 2019;4(1):29.
[3] Gong CX, Liu F, Iqbal K. Multifactorial hypothesis and multi-targets for Alzheimer's diseas. J Alzheimer's Dis 2018;64:S107–17.
[4] Morimoto BH. Therapeutic peptides for CNS indications: progress and challenges. Bioorg Med Chem 2018;26(10):2859–62.
[5] He S, Duan C, Wang S, Yu Y, Kei Chan Y, Shi X, et al. Fusion peptide-engineered polyetheretherketone implants with photo-assisted anti-pathogen and enhanced angiogenesis for *in vivo* osseointegrative fixation. Chem Eng J 2022;446:137453.
[6] Lalatsa A, Schatzlein AG, Uchegbu IF. Strategies to deliver peptide drugs to the brain. Mol Pharm 2014;11(4):1081–93.
[7] Ghosh D, Peng X, Leal J, Mohanty RP. Peptides as drug delivery vehicles across biological barriers. J Pharm Invest 2018;48(1):89–111.
[8] Mickan A, Sarko D, Haberkorn U, Mier W. Rational design of CPP-based drug delivery systems: considerations from pharmacokinetics. Curr Pharm Biotechnol 2014;15(3):200–9.
[9] Yuan L, Liu XJ, Han WN, Li QS, Wang ZJ, Wu MN, et al. [Gly14]-Humanin protects against amyloid β peptide-induced impairment of spatial learning and memory in rats. Neurosci Bull 2016;32(4):374–82.
[10] Chin YP, Keni J, Wan JX, Mehta H, Anene F, Jia Y, et al. Pharmacokinetics and tissue distribution of Humanin and its analogues in male rodents. Endocrinology 2013;154(10):3739–44.
[11] Xu X, Chua CC, Gao J, Chua KW, Wang H, Hamdy RC, et al. Neuroprotective effect of humanin on cerebral ischemia/reperfusion injury is mediated by a PI3K/Akt pathway. Brain Res 2008;1227:12–18.
[12] Alsanousi N, Sugiki T, Furuita K, So M, Lee YH, Fujiwara T, et al. Solution NMR structure and inhibitory effect against amyloid-β fibrillation of Humanin containing a D-isomerized serine residue. Biochem Biophys Res Commun 2016;477(4):647–53.
[13] Milletti F. Cell-penetrating peptides: classes, origin, and current landscape. Drug Discov Today 2012;17(15):850–60.
[14] Kardani K, Milani A, Shabani S H, Bolhassani A. Cell penetrating peptides: the potent multi-cargo intracellular carriers. Expert Opin Drug Delivery 2019;16(11):1227–58.
[15] Szeto HH. Cell-permeable, mitochondrial-targeted, peptide antioxidants. AAPS J 2006;8(2):32.
[16] Ragin AD, Morgan RA, Chmielewski J. Cellular import mediated by nuclear localization signal peptide sequences. Chem Biol 2002;9(8):943–8.
[17] Qian K, Bao X, Li Y, Wang P, Guo Q, Yang P, et al. Cholinergic neuron targeting nanosystem delivering hybrid peptide for combinatorial mitochondrial therapy in Alzheimer's disease. ACS Nano 2022;16(7):11455–72.
[18] Esposito L, Balasco N, Smaldone G, Berisio R, Ruggiero A, Vitagliano L. AlphaFold-Predicted structures of KCTD proteins unravel previously undetected relationships among the members of the family. Biomolecules 2021;11(12):1862.
[19] Klimpel A, Neundorf I. Bifunctional peptide hybrids targeting the matrix of mitochondria. J Control Release 2018;291:147–56.
[20] Benaki D, Zikos C, Evangelou A, Livaniou E, Vlassi M, Mikros E, Pelecanou M. Solution structure of humanin, a peptide against Alzheimer's disease-related neurotoxicity. Biochem Biophys Res Commun 2005;329(1):152–60.
[21] Song J, Kai M, Zhang W, Zhang J, Liu L, Zhang B, et al. Cellular uptake of transportan 10 and its analogs in live cells: selectivity and structure–activity relationship studies. Peptides 2011;32(9):1934–41.
[22] Jumper J, Evans R, Pritzel A, Green T, Figurnov M, Ronneberger O, et al. Highly accurate protein structure prediction with AlphaFold. Nature 2021;596(7873):583–9.
[23] Tararina MA, Yee DA, Tang Y, Christianson DW. Structure of the repurposed fungal terpene cyclase FlvF implicated in the C-N bond-forming reaction of flavunoidine biosynthesis. Biochemistry 2022;61(18):2014–24.
[24] Obita T, Inaka K, Kohda D, Maita N. Crystal structure of the PX domain of Vps17p from Saccharomyces cerevisiae. Acta Cryst F Struct Biol Commun 2022;78:210–16 Pt 5.
[25] Benaki D, Zikos C, Evangelou A, Livaniou E, Vlassi M, Mikros E, et al. Solution structure of Ser14Gly-humanin, a potent rescue factor against neuronal cell death in Alzheimer's disease. Biochem Biophys Res Commun 2006;349(2):634–42.
[26] Chen L, Zhang Q, Yuan X, Cao Y, Yuan Y, Yin H, et al. How charge distribution influences the function of membrane-active peptides: lytic or cell-penetrating? Int J Biochem Cell Biol 2017;83:71–5.

[27] Biverståhl H, Andersson A, Gräslund A, Mäler L. NMR solution structure and membrane interaction of the N-terminal sequence (1–30) of the bovine prion protein. Biochemistry 2004;43(47):14940–7.
[28] Oglęcka K, Lundberg P, Magzoub M, LE Göran Eriksson, Ü Langel, Gräslund A. Relevance of the N-terminal NLS-like sequence of the prion protein for membrane perturbation effects. Biochim Biophys Acta, Biomembr 2008;1778(1):206–13.
[29] Ramsey JD, Flynn NH. Cell-penetrating peptides transport therapeutics into cells. Pharmacol Ther 2015;154:78–86.
[30] Ruseska I, Zimmer A. Internalization mechanisms of cell-penetrating peptides. Beilstein J Nanotechnol 2020;11:101–23.
[31] Zhao K, Luo G, Giannelli S, Szeto HH. Mitochondria-targeted peptide prevents mitochondrial depolarization and apoptosis induced by tert-butyl hydroperoxide in neuronal cell lines. Biochem Pharmacol 2005;70(12):1796–806.
[32] Madreiter-Sokolowski CT, Thomas C, Ristow M. Interrelation between ROS and Ca^{2+} in aging and age-related diseases. Redox Biol 2020;36:101678.
[33] Peng X, Wang K, Zhang C, Bao JP, Vlf C, Gao JW, et al. The mitochondrial antioxidant SS-31 attenuated lipopolysaccharide-induced apoptosis and pyroptosis of nucleus pulposus cells via scavenging mitochondrial ROS and maintaining the stability of mitochondrial dynamics. Free Radical Res 2021;55(11–12):1080–93.
[34] Klein LE, Cui L, Gong Z, Su K, Muzumdar R. A humanin analog decreases oxidative stress and preserves mitochondrial integrity in cardiac myoblasts. Biochem Biophys Res Commun 2013;440(2):197–203.
[35] Szeto HH, Schiller PW. Novel therapies targeting inner mitochondrial membrane—From discovery to clinical development. Pharm Res 2011;28(11):2669–79.
[36] Hashimoto Y, Kurita M, Aiso S, Nishimoto I, Matsuoka M. Humanin inhibits neuronal cell death by interacting with a cytokine receptor complex or complexes involving CNTF receptor α/WSX-1/gp130. Mol Biol Cell 2009;20(12):2864–73.
[37] Sompol P, Ittarat W, Tangpong J, Chen Y, Doubinskaia I, Batinic-Haberle I, et al. A neuronal model of Alzheimer's disease: an insight into the mechanisms of oxidative stress-mediated mitochondrial injury. Neuroscience 2008;153(1):120–30.
[38] Singulani MP, Pereira CPM, Ferreira AFF, Garcia PC, Ferrari GD, Alberici LC, et al. Impairment of PGC-1α-mediated mitochondrial biogenesis precedes mitochondrial dysfunction and Alzheimer's pathology in the 3xTg mouse model of Alzheimer's disease. Exp Gerontol 2020;133:110882.
[39] Sheshadri P, Ashwini A, Jahnavi S, Bhonde R, Prasanna J, Kumar A. Novel role of mitochondrial manganese superoxide dismutase in STAT3 dependent pluripotency of mouse embryonic stem cells. Sci Rep 2015;5(1):9516.
[40] Wegrzyn J, Potla R, Chwae YJ, Sepuri NB, Zhang Q, Koeck T, et al. Function of mitochondrial Stat3 in cellular respiration. Science (1979) 2009;323(5915):793–7.
[41] Jung JE, Kim GS, Narasimhan P, Song YS, Chan PH. Regulation of Mn-superoxide dismutase activity and neuroprotection by STAT3 in mice after cerebral ischemia. J Neurosci 2009;29(21):7003–14.
[42] Hampel H, Hardy J, Blennow K, Chen C, Perry G, Kim SH, et al. The amyloid-β pathway in Alzheimer's disease. Mol Psychiatry 2021;26(10):5481–503.
[43] Trott O, Olson AJ. AutoDock Vina: improving the speed and accuracy of docking with a new scoring function, efficient optimization, and multithreading. J Comput Chem 2010;31(2):455–61.
[44] Upadhaya AR, Lungrin I, Yamaguchi H, Fändrich M, Thal DR. High-molecular weight Aβ oligomers and protofibrils are the predominant Aβ species in the native soluble protein fraction of the AD brain. J Cell Mol Med 2012;16(2):287–95.
[45] Yasumoto T, Takamura Y, Tsuji M, Nakayama T, Imamura K, Inoue H, et al. High molecular weight amyloid β1-42 oligomers induce neurotoxicity via plasma membrane damage. Alzheimer's Dementia 2020;16(S2):e037546.
[46] Wiatrak B, Piasny J, Kuźniarski A, Gąsiorowski K. Interactions of amyloid-β with membrane proteins. Int J Mol Sci 2021;22(11):6075.
[47] Marta R, Rebecca P, Muriel JS, Sylvie B, Robin R-D, Jose M-H, et al. Effect of Aβ oligomers on neuronal APP triggers a vicious cycle leading to the propagation of synaptic plasticity alterations to healthy neurons. J Neurosci 2020;40(27):5161.
[48] Ribeiro MF, Genebra T, Rego AC, Rodrigues CMP, Solá S. Amyloid β peptide compromises neural stem cell fate by irreversibly disturbing mitochondrial oxidative state and blocking mitochondrial biogenesis and dynamics. Mol Neurobiol 2019;56(6):3922–36.
[49] Nizami S, Hall-Roberts H, Warrier S, Cowley SA, Di Daniel E. Microglial inflammation and phagocytosis in Alzheimer's disease: potential therapeutic targets. Br J Pharmacol 2019;176(18):3515–32.
[50] Anwar S, Rivest S. Alzheimer's disease: microglia targets and their modulation to promote amyloid phagocytosis and mitigate neuroinflammation. Expert Opin Ther Targets 2020;24(4):331–44.
[51] Murakami M, Nagahama M, Abe Y, Niikura T. Humanin affects object recognition and gliosis in short-term cuprizone-treated mice. Neuropeptides 2017;66:90–6.
[52] Heneka MT, Kummer MP, Stutz A, Delekate A, Schwartz S, Vieira-Saecker A, et al. NLRP3 is activated in Alzheimer's disease and contributes to pathology in APP/PS1 mice. Nature 2013;493(7434):674–8.
[53] Liu Y, Dai Y, Li Q, Chen C, Chen H, Song Y, et al. Beta-amyloid activates NLRP3 inflammasome via TLR4 in mouse microglia. Neurosci Lett 2020;736:135279.
[54] D'Hooge R, De Deyn PP. Applications of the Morris water maze in the study of learning and memory. Brain Res Rev 2001;36(1):60–90.
[55] Welikovitch LA, Do Carmo S, Maglóczky Z, Malcolm JC, Lőke J, Klein WL, et al. Early intraneuronal amyloid triggers neuron-derived inflammatory signaling in APP transgenic rats and human brain. Proc Natl Acad Sci USA 2020;117(12):6844–54.
[56] Maturana P, Martinez M, Noguera ME, Santos NC, Disalvo EA, Semorile L, et al. Lipid selectivity in novel antimicrobial peptides: implication on antimicrobial and hemolytic activity. Colloids Surf, B 2017;153:152–9.
[57] Saar K, Lindgren M, Hansen M, Eiríksdóttir E, Jiang Y, Rosenthal-Aizman K, et al. Cell-penetrating peptides: a comparative membrane toxicity study. Anal Biochem 2005;345(1):55–65.
[58] Işeri S, Ercan F, Gedik N, Yüksel M, Alican I. Simvastatin attenuates cisplatin-induced kidney and liver damage in rats. Toxicology 2007;230(2–3):256–64.